A Spreading Drop of Shallow Water

Dorota Jarecka[a,b,*], Anna Jaruga[a], Piotr K. Smolarkiewicz[c]

[a] *Institute of Geophysics, Faculty of Physics, University of Warsaw, Poland*
[b] *National Center for Atmospheric Research, USA*
[c] *European Centre for Medium-Range Weather Forecasts, UK*

Abstract

The theoretical solutions and corresponding numerical simulations of [Schär & Smolarkiewicz, J. Comput. Phys, 128 (1996) 101]) are revisited. The original abstract problem of a parabolic, slab-symmetric drop of shallow water spreading under gravity is extended to three spatial dimensions, with the initial drop defined over an elliptical compact support. An axisymmetric drop is considered as a special case. The elliptical drop exhibits enticing dynamics, which may appear surprising at the first glance. In contrast, the evolution of the axisymmetric drop is qualitatively akin to the evolution of the slab-symmetric drop and intuitively obvious. Besides being interesting per se, the derived theoretical results provide a simple means for testing numerical schemes concerned with wetting-drying areas in shallow water flows. Reported calculations use the *libmpdata++*, a recently released free/libre and open-source software library of solvers for generalized transport equations. The numerical results closely match theoretical predictions, demonstrating strengths of the nonoscillatory forward-in-time integrators comprising the *libmpdata++*.

Keywords: shallow-water equations, wetting-drying areas, monotonicity preserving advection schemes, MPDATA

*Corresponding author: Dorota Jarecka, National Center for Atmospheric Research, 3090 Center Green Drive, Boulder, CO 80301, +1 303 497 8219

Email address: dorota@igf.fuw.edu.pl (Dorota Jarecka)

1. Introduction

The "shallow water equations"(SWE) is a popular topic in the Journal of Computational Physics (JCP). According to the Thomson Reuters Web of Science, nearly 300 papers on SWE have been published in JCP since 1971 ($\approx$ 4% of all recorded SWE papers published since 1969), with the accrued citation count approaching 7000 ($\approx$ 6% of all recorded citations). The SWE attract interdisciplinary interests, as substantiated by numerous contributions in the areas of applied mathematics, astrophysics, environmental engineering, fluid dynamics, geophysics, meteorology and oceanography. Apart from providing a practical long-wave approximation for PDE systems governing, in general, continuously-stratified 3D flows [1, 2], SWE also provide a convenient testing ground for development of numerical methods and complex models in a broad range of computational science and engineering.

The work [3] is a representative example amid those using SWE to prove new developments. In [3] the authors addressed the compatibility of Eulerian and Lagrangian numerical integrations of coupled transport equations, in the context of geophysical flows. One of the computational testbeds employed to quantify the accuracy of the proposed schemes was an idealized problem of a 2D slab-symmetric drop of shallow water spreading under gravity. While directly addressing the wetting-drying areas for the SWE, this problem also epitomizes inflating-collapsing material layers in isentropic/isopycnic models for atmospheric/oceanic circulations. Technically, such models resemble a stack of shallow water models, coupled by the hydrostacy in the vertical direction [3, 4]. Just like in conservative integrations of SWE, diagnosing velocity in material layers may require calculating ratios of the momentum and the layer depth. Preventing this division from becoming ill-defined requires the momentum and the layer depth to vanish compatibly; i.e., with their ratio always being well defined, as implied by the evolutionary (Lagrangian) form of the specific momentum equation (velocity).

Here, we extend the theoretical solutions of [3] to 3D drops with an elliptical compact support, the axisymmetric case of which is described by particularly concise and elegant formulae. The theoretical results provide simple means of quantifying the accuracy of multidimensional schemes required to deal with wetting-drying areas and inflating-collapsing material layers. Theoretical predictions are supplemented with numerical integrations of partial differential SWE using the MPDATA-based nonoscillatory forward-in-time methods, also used in [3] and widely documented in the literature; see [5]

for a recent summary. All simulations were performed using *libmpdata++*, a free/libre and open-source software library of solvers for generalized transport equations [6]. The corresponding theoretical and computational results corroborate each other.

The paper is organized as follows. Section 2 presents the problem, summarizes analytical derivations, and discusses theoretical results. Section 3 highlights numerical integrators and compares theoretical and computational results. Remarks in section 4 conclude the paper.

2. Analytical results

2.1. Problem statement

Following [3], the addressed physical scenario consist of an initially stagnant lenticular drop of a homogeneous incompressible inviscid fluid that spreads under gravity on the plane, in absence of friction and background rotation.[1] The depth-integrated governing PDE postulate the shallow-water (hydrostatic) approximation, physically sound when the width of the drop significantly exceeds its height. Conforming to the formulation in [3], the extended 2D SWE take the dimensionless form

$$\partial_t h + \partial_x(uh) + \partial_y(vh) = 0 \ , \tag{1}$$

$$\partial_t(uh) + \partial_x(uuh) + \partial_y(vuh) = -h\partial_x h \ , \tag{2}$$

$$\partial_t(vh) + \partial_x(uvh) + \partial_y(vvh) = -h\partial_y h \ , \tag{3}$$

where h, (u, v), (x, y) and t have the usual meaning of height, velocity components, Cartesian coordinates and time. The indicated variables are normalized, respectively, by a characteristic height scale h_o, the celerity $u_o = (gh_o)^{1/2}$ (with g denoting the gravitational acceleration), a characteristic width scale a, and the characteristic time scale $t_o = a/u_o$.

In contrast to the 1D formulation of [3] — in turn inspired by the study of a SWE ribbon on a rotating plane [7] — our initial drop is defined over an elliptical compact support on the xy plane

$$\begin{aligned} h(x, y, t = 0) &> 0 \ \text{ if } \ \frac{x^2}{\lambda_{x0}^2} + \frac{y^2}{\lambda_{y0}^2} < 1 \ , \\ h(x, y, t = 0) &= 0 \ \text{ otherwise} \ , \end{aligned} \tag{4}$$

[1] Surface tension effects are irrelevant for applications addressed in this paper.

where λ_{x0} and λ_{y0} are the major and minor semi-axes of the ellipse. Following the earlier works [3, 7, 8], the solutions are sought to maintain parabolic profiles in the x and y cuts, so the evolving height can be written as

$$\begin{aligned} h(x,y,t) &= A(\lambda_x,\lambda_y)(1-\frac{x^2}{\lambda_x^2}-\frac{y^2}{\lambda_y^2}) \ \text{ if } \ \frac{x^2}{\lambda_x^2}+\frac{y^2}{\lambda_y^2}<1\ , \\ h(x,y,t) &= 0 \ \text{ otherwise }, \end{aligned} \tag{5}$$

where $\lambda_x(t)$ and $\lambda_y(t)$ depend solely on time, while the actual height of the drop at the origin $A(\lambda_x,\lambda_y)>0 \ \ \forall\ t<\infty$. The theoretical results for the general case of (5) will be presented next, whereas the special axisymmetric case, $\lambda_x=\lambda_y\ \forall\ t$, will be presented in section 2.3.

2.2. Elliptical drops

Along the $y=0$ and $x=0$ symmetry axes the solution is expected to retain the key functional dependencies of the 1D case [3]. Consequently, we postulate $A(\lambda_x,\lambda_y)=\lambda_x^n\lambda_y^n$ in (5), where the exponent $n<0$ is yet to be determined. Furthermore, it is also assumed that the velocities change linearly across the drop and satisfy $u(\lambda_x,t)=d\lambda_x/dt\equiv\dot{\lambda}_x$, and $v(\lambda_y,t)=d\lambda_y/dt\equiv\dot{\lambda}_y$ at the x and y edges of the drop, respectively. The simplest form that fulfills these requirements is the irrotational flow

$$u(x,t)=x\frac{\dot{\lambda}_x}{\lambda_x}\ , \quad v(y,t)=y\frac{\dot{\lambda}_y}{\lambda_y}\ . \tag{6}$$

After inserting (5) and (6) in (1), the result shows that the mass continuity equation is satisfied only if $n=-1$; i.e. $A(\lambda_x,\lambda_y)=1/(\lambda_x\lambda_y)$. Furthermore, inserting the postulated forms for $u(x,t)$, $v(x,t)$ and $h(x,y,t)$ into (2), (3) and manipulating the algebra, reveals the autonomous system of two nonlinear second-order ODEs

$$\ddot{\lambda}_x=\frac{2}{\lambda_x^2\lambda_y}\ , \quad \ddot{\lambda}_y=\frac{2}{\lambda_x\lambda_y^2}\ . \tag{7}$$

Introducing two auxiliary variables $\beta_x\equiv\dot{\lambda}_x$ and $\beta_y\equiv\dot{\lambda}_y$ allows to rewrite (7) as a system of four first-order ODEs that can be numerically integrated with high precision using, e.g., an implementation of the LSODA method from the ODEPACK library; see [9] for the method description. Such semi-analytical solutions to the SWE (1)-(3) are presented in Fig. 1.

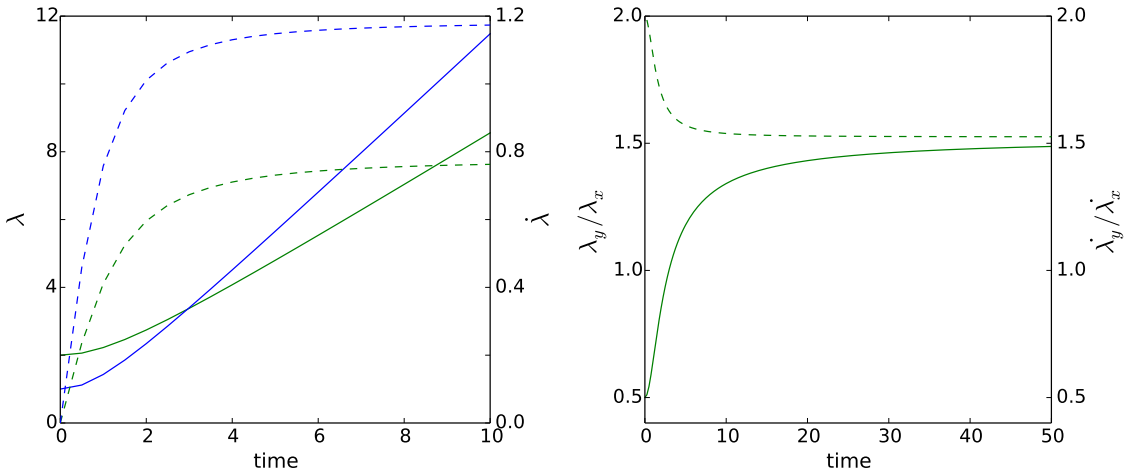

Figure 1: Left, the history of semi-axes λ_x, λ_y (solid lines) and their respective spreading rates $\dot{\lambda}_x$, $\dot{\lambda}_y$ (dashed lines). Right, the long-time history of the ratios λ_y/λ_x and $\dot{\lambda}_y/\dot{\lambda}_x$.

The left panel of Fig. 1 documents the evolution of the semi-axes ($\lambda_x,\ \lambda_y$) and their respective spreading rates ($\dot{\lambda}_x,\ \dot{\lambda}_y$) starting from the initial values ($\lambda_{x0} = 2, \lambda_{y0} = 1$) at rest. Both axes increase with time, but as a consequence of their second-derivative forms (7), the initially minor axis λ_y increases faster than the major axis λ_x, and this leads to the equalization of axes at $t \gtrsim 3$. The circular shape is, however, transient since the velocities of the ellipse's edges in both directions are different, and the initially minor and major axes swap their roles. Furthermore, Fig. 1 shows that the velocities tend to their asymptotic values relatively fast, while the axes increase linearly, so the shape of the ellipse with swapped axes is preserved. For completeness, the right panel of Fig. 1 shows the asymptotic behaviors of the ratio of axes and their spreading rates (note fivefold time compared to the left panel). Noteworthy, although the ratios λ_x/λ_y and $\ddot{\lambda}_x/\ddot{\lambda}_y$ cross unity (recall eqs. 7), the ratio $\dot{\lambda}_x/\dot{\lambda}_y$ does not.

Further theoretical estimates for the drop geometry in function of time can be inferred from the energy considerations. We begin with the differential relations for the potential and kinetic energies — cf. section 3.6.2 in [10] — of the SWE (1)-(3)

$$\mathrm{d}E_{pot} = \frac{1}{2} h(x,y)\ \mathrm{d}m\ , \tag{8}$$

$$\mathrm{d}E_{kin} = \frac{1}{2}\left(u(x)^2 + v(y)^2\right)\ \mathrm{d}m\ , \tag{9}$$

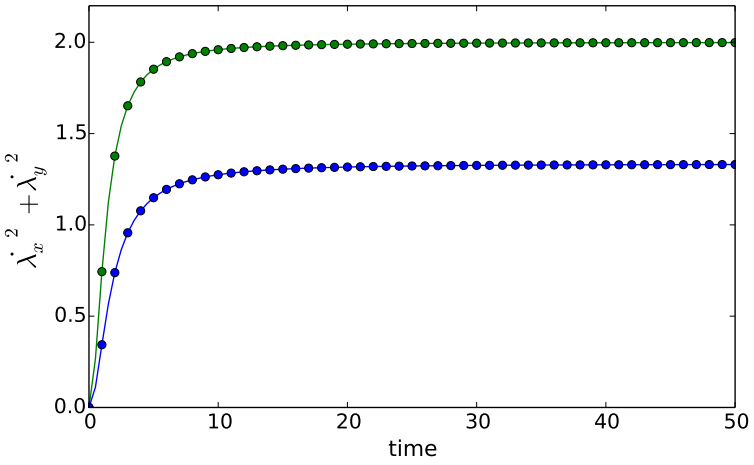

Figure 2: History of the LHS (solid lines) and RHS (circles) of (14) for two initial conditions $\lambda_{x0} = 2$ (green) and $\lambda_{x0} = 3$ (blue) with $\lambda_{y0} = 1$ in both cases.

where

$$\mathrm{d}m = h(x,y)\ \mathrm{d}x\mathrm{d}y = \frac{1}{\lambda_x \lambda_y}\left(1 - \frac{x^2}{\lambda_x^2} - \frac{y^2}{\lambda_y^2}\right)\ \mathrm{d}x\mathrm{d}y\ , \tag{10}$$

denotes the mass in the column with height $h(x,y)$ and infinitesimal horizontal area. Integrating the resulting expressions over the volume of the drop, leads to the following result (see Appendix A)

$$E_{pot} = \frac{\pi}{6}\frac{1}{\lambda_x \lambda_y}\ , \tag{11}$$

$$E_{kin} = \frac{\pi}{24}\left((\dot{\lambda}_x)^2 + (\dot{\lambda}_y)^2\right)\ . \tag{12}$$

The energy conservation for the case at hand

$$E_{pot} + E_{kin} = E_{pot}(t=0)\ , \tag{13}$$

together with (11) and (12), implies

$$(\dot{\lambda}_x)^2 + (\dot{\lambda}_y)^2 = 4\left(\frac{1}{\lambda_{x0}\lambda_{y0}} - \frac{1}{\lambda_x \lambda_y}\right) \tag{14}$$

that is consistent with (7).[2]

[2]Differentiating (14) with respect to time, and using (7) on the LHS results in the identity.

The relation (14) verifies the semi-analytical results from the integrations using the ODEPACK library. Figure 2 presents both sides of (14) — marking left- and right-hand side with solid lines and circles, respectively — for two initial conditions $\lambda_{x0} = 2$ and $\lambda_{x0} = 3$ with the fixed $\lambda_{y0} = 1$. Indeed, both sides of the equation match each other closely tending to the asymptotic value $4/(\lambda_{x0}\lambda_{y0})$, i.e. to 2 and 4/3 for the two presented cases.

2.3. Axisymmetric drops

For the special case of $\lambda_x = \lambda_y \equiv \lambda \ \ \forall\, t$, the solution for general case of (5) and (6), takes a simpler form

$$h(x,y,t) = \frac{1}{\lambda^2}\left(1 - \frac{x^2+y^2}{\lambda^2}\right) , \tag{15}$$

$$u(x,t) = x\frac{\dot{\lambda}}{\lambda} , \quad v(y,t) = y\frac{\dot{\lambda}}{\lambda} , \tag{16}$$

whereas the second derivative expressions (7) reduce to

$$\ddot{\lambda} = \frac{2}{\lambda^3} . \tag{17}$$

It can be shown that these equations satisfy (1)-(3). Because the dependence of the second derivative (17) on λ is much simpler than for general case, the complete analytical solution can be easily derived.

Defining an auxiliary variable $\beta(\lambda) \equiv \dot{\lambda}$, (17) can be rewritten as

$$\ddot{\lambda} = \frac{d\beta}{d\lambda}\dot{\lambda} = \frac{d\beta}{d\lambda}\beta = \frac{1}{2}\frac{d(\beta^2)}{d\lambda} = \frac{2}{\lambda^3} . \tag{18}$$

Integrating the last equality in (18) for β^2 leads to

$$\beta^2\big|_{t_0}^{t} = -\frac{2}{\lambda^2}\bigg|_{t_0}^{t} , \tag{19}$$

while accounting for the initial conditions produces[3]

$$\dot{\lambda}(t) = \beta(t) = \sqrt{2\left(\frac{1}{\lambda_0^2} - \frac{1}{\lambda(t)^2}\right)} . \tag{20}$$

[3]The same relation can be obtained from (14), if λ_x and λ_y are substituted for λ.

Manipulating the algebra and integrating (20) gives the closed-form solution for drop radius evolution

$$\lambda(t) = \sqrt{2t^2 + \lambda_0^2} \tag{21}$$

Finally, inserting (21) to (15) and (16) straightforwardly leads to closed-form solutions for the actual height of, and the velocity field within the drop.

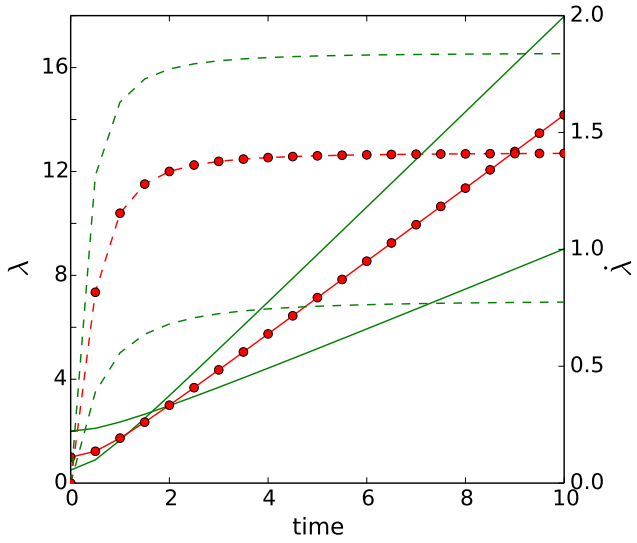

Figure 3: History of axisymmetric drop radius, λ, (red solid line) and its corresponding spreading rate, $\dot{\lambda}$, (red dashed lines). The lines present a semi-analytical solution obtained from solving (7) using ODEPACK for axisymmetric initial condition $\lambda_{x0} = \lambda_{y0} = 1$. The dots indicate a closed-form analytical solution obtained from (21). The green lines present time evolutions of axes (solid lines) and their corresponding spreading rates (dashed lines) for elliptical drop with the same initial energy as for the axisymmetric drop ($\lambda_{x0} = 2$ and $\lambda_{y0} = 0.5$).

Figure 3 presents two solutions for the axisymmetric drop with the initial radius $\lambda_0 = 1$. Red lines present the results using numerical ODEPACK integrations, as it was done for the elliptic case, with solid and dashed lines marking λ and $\dot{\lambda}$, respectively. Red circles indicate the closed-form analytical solutions. For comparison, green lines present results for elliptic drop with $\lambda_{x0} = 2$ and $\lambda_{y0} = 1/2$; i.e., with the same potential energy as for the axisymmetric drop.

The next section compares the theoretical predictions with numerical simulations of partial-differential SWE (1)-(3).

3. Numerical results

3.1. Approach

Numerical integrations of the governing PDEs (1)-(3) presented in this paper employ the *libmpdata++* — a collection of parallel numerical algorithms for solving generalized inhomogeneous advection transport equations. The *libmpdata++* has been recently released as free/libre open-source software library and is available at `http://libmpdataxx.igf.fuw.edu.pl/` . The implementation concepts, the library documentation, and a range of examples can be found in [6]. The algorithms in the *libmpdata++* implement MPDATA (for multidimensional positive-definite advection transport algorithm) — a class of nonoscillatory forward-in-time flux-form schemes already well reviewed in the literature, see [11, 12, 5] and references therein.[4] The numerical simulations presented in this paper use exclusively the second-order accurate **fct+iga+dfl+trapez** option of *libmpdata++* with the **vip_eps** set arbitrarily to 10^{-7}. That is, the monotonicity preserving infinite-gauge option of MPDATA for elastic/compressible flows, with the trapezoidal integral of the RHS in the momentum equations and the residual depth of the fluid set to 10^{-7} while evaluating the velocity components from momenta and depth; see sections 5.3, 5.4 in [6].

In algorithmic terms, the approach specified above can be compactly written as

$$h_i^{n+1} = \mathcal{A}_i\left(h^n, \mathbf{V}^{n+1/2}\right) , \tag{22}$$

$$q_x|_i^{n+1} = \mathcal{A}_i\left(\widetilde{q_x}, \mathbf{V}^{n+1/2}\right) - 0.5\delta t(h\partial_x h)|_i^{n+1} , \tag{23}$$

$$q_y|_i^{n+1} = \mathcal{A}_i\left(\widetilde{q_y}, \mathbf{V}^{n+1/2}\right) - 0.5\delta t(h\partial_y h)|_i^{n+1} , \tag{24}$$

where i marks the nodes of a co-located regular grid, $n = 0, 1, 2, ..$ denotes the temporal level, and $\mathcal{A}$ symbolizes the advective transport operator; here, the MPDATA advection scheme. The depth of the fluid h and momentum vector $\mathbf{q} = (q_x, q_y)$ are the dependent variables defined initially and evolved with the algorithmic relations (22)-(24). The velocity $\mathbf{V}_i^n$ — calculated as $\mathbf{V}_i^n = \mathbf{q}_i^n / h_i^n$ if $h_i^n > \epsilon$, and $\mathbf{V}_i^n = 0$ otherwise (here, $\epsilon = 10^{-7}$) — is extrapolated linearly

[4] MPDATA is iterative in nature. Each iteration is a simple upwind scheme that is conservative, sign-preserving and free of directional splitting, but only first-order accurate. Subsequent iterations compensate the leading errors of the preceding iterations using a pseudo-velocity field derived from truncation errors of upwind differencing.

from its $t^{n-1} = (n-1)\delta t$ and $t^n = n\delta t$ values to $t^{n+1/2}$ and interpolated linearly to the cell-walls encompassing the node i, to provide the advecting velocity field $\mathbf{V}^{n+1/2}$ for MPDATA. The advecting velocity is the same for all advected variables; i.e., h and the auxiliary momenta $\widetilde{\mathbf{q}} \equiv \mathbf{q}^n - 0.5\delta t(h\nabla h)^n$. Given a second-order-accurate $\mathcal{A}$ and smooth data, the resulting integrator in (22)-(24) provides second-order-accurate solutions for the SWE (1)-(3); see section 4.1 in [4] for a demonstration.

3.2. Solutions

Figures 4 and 5 highlight the numerical results obtained by using *libmpdata++* for the spreading elliptical drop,[5] corresponding to the theoretical solutions discussed in section 2.2. The parameters of the reference simulation are as follows. The time step is set to $\delta t = 0.01$ and the gridsize to $\delta x = \delta y = 0.05$. The computational domain consist of 400×400 grid cells. The initial conditions assume zero velocity and ($\lambda_{x0} = 2$, $\lambda_{y0} = 1$). Figure 4 shows the height of the drop at the times: $t = 0, 1, 3, 7$, with superimposed velocity vectors. Figure 5 shows the corresponding velocity field, $(u^2+v^2)^{1/2}$, at $t = 3$ and 7.

Figure 4 documents that the initially minor axis λ_y increases faster than the major axis λ_x. In consequence, at $t = 3$, the two axes nearly equal each other, and at later times λ_y becomes a major axis. Figure 5 corroborates this result, showing that at $t = 3$ the spreading rate $\dot{\lambda}_y$ is larger than the spreading rate $\dot{\lambda}_x$. In fact, the $\dot{\lambda}_y > \dot{\lambda}_x$ for the entire simulation, consistent with the semi-analytical results of section 2.2.

Figure 6 complements Figs. 4 and 5 with the display of the cuts along the two main axes of the elliptical drop. As illustrated in the figures, the model results are free of any apparent oscillations near the drop edge and are in good agreement with analytical results.

To provide quantitative measure of the model accuracy, Table 1 lists norms of the leading truncation errors at $t = 7$ for the reference simulation supplemented with coarsened and refined calculations. The error norms are defined as follows

$$\| \delta h \|_\infty \equiv \frac{\max\Big(|h_{num} - h_{an}|\Big)}{\max\Big(h_{an}(t=0)\Big)} , \tag{25}$$

[5]The solution for the axisymmetric drop is analyzed in sec. 5.4 of [6].

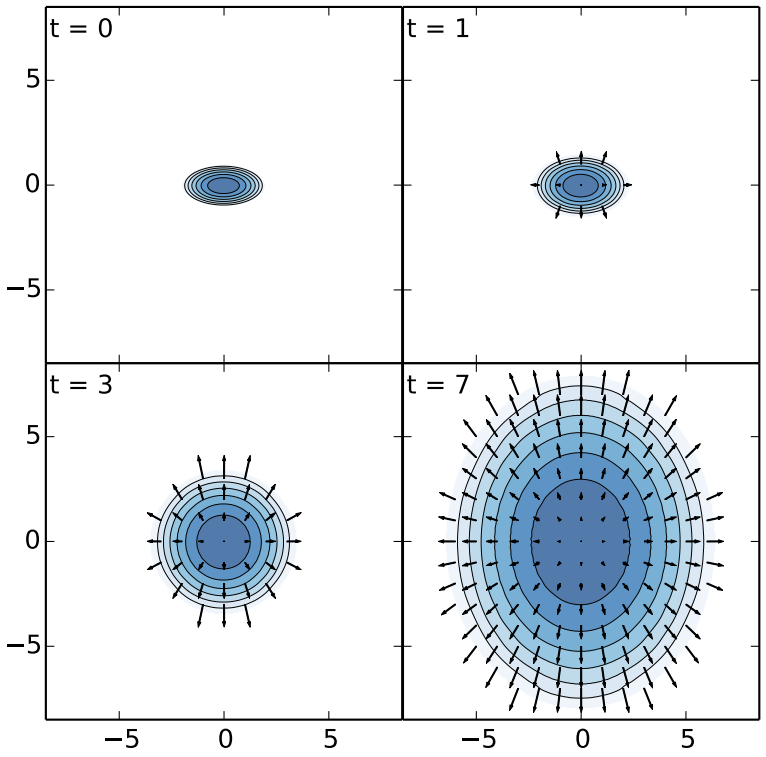

Figure 4: Height of the drop with superimposed velocity vectors, projected on the xy plane, at $t = 0, 1, 3$ and 7; contour intervals are evenly spaced between 0 and the maximum values 0.50, 0.31, 0.09 and 0.02 for $t = 0, 1, 3$ and 7, respectively.

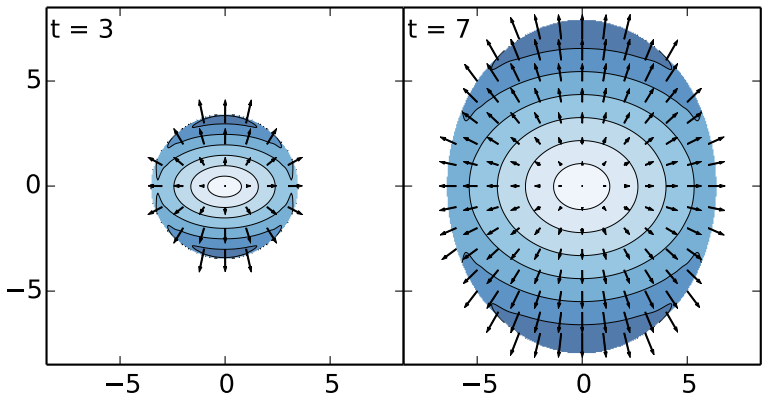

Figure 5: As in Fig. 4 but for the total velocity at $t = 3$ and $t = 7$; the contours are drawn with seven 0.16 intervals between 0 and 1.12.

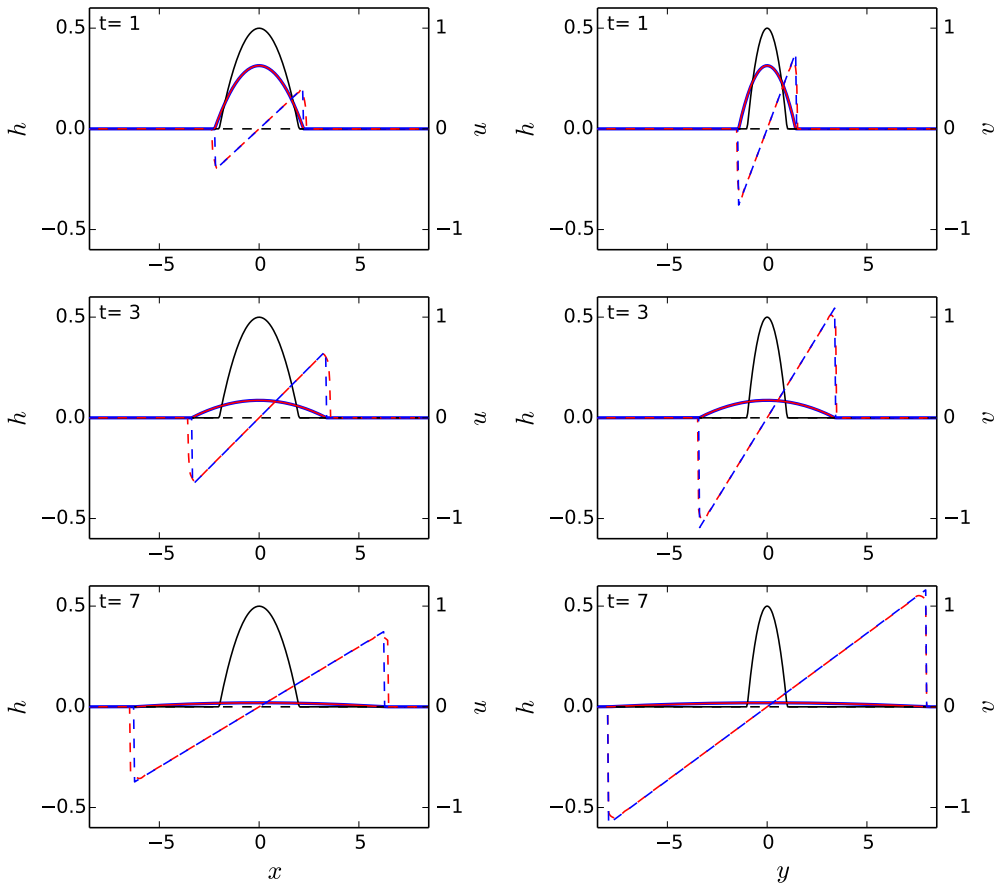

Figure 6: The model and theoretical results in the x and y cuts for $t = 1, 3$ and 7. Solid and dashed lines represent, respectively, the height and the velocity component tangential to the cut. The initial condition is plotted in black, analytical solution in blue and numerical results in red; for the height, the analytical and numerical solutions are hardly distinguishable.

$$\| \delta h \|_2 \equiv \frac{1}{t}\sqrt{\frac{1}{N}\sum_{i=1}^{N}(h_{num} - h_{an})^2}\ , \tag{26}$$

where h_{num} and h_{an} denote, respectively, the model results and the corresponding theoretical solutions in N gridpoints (x_i, y_i) at an instant t. While (25) measures the maximal solution error accumulated over time t, (26) is a measure of the truncation error in approximating the PDE. The table documents first-order convergence in the both norms — similar result has been

obtained for the total velocity (not shown). The first-order convergence is adequate since the solution lacks smoothness at the drop edge, Fig. 6. Indeed, Fig. 7 confirms that the truncation error is concentrated at the edge. Furthermore, Table 2 documents that the error decreases with time, which is consistent with Fig. 6 that implies diminishing discontinuity of spatial derivatives of h at the edge as the drop spreads.

δx / δt	0.1 / 0.02	0.05 / 0.01	0.025 / 0.005	0.0125 / 0.0025
$\| \delta h \|_{\text{inf}}$	3.88 e-3	1.85 e-3	0.84 e-3	0.38 e-3
$\| \delta h \|_2$	4.24 e-5	1.47 e-5	0.59 e-5	0.26 e-5

Table 1: The convergence of the error norms (25) and (26) at $t = 7$. The third column corresponds to the reference simulation with $\delta x = 0.05$ and $\delta t = 0.01$.

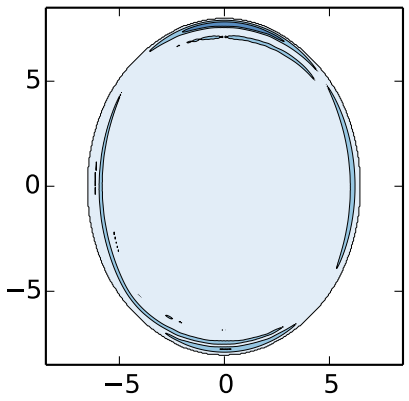

Figure 7: The field of truncation error $|h_{num} - h_{an}| / \max\left(h_{an}(t=0)\right)$ for the reference simulation at $t = 7$. The contours are drawn with three evenly spaced intervals between 0 and 2 e-3.

t	1	3	7
$\| \delta h \|_{\text{inf}}$	3.61 e-2	0.82 e-2	0.18 e-2
$\| \delta h \|_2$	1.05 e-3	0.10 e-3	0.01 e-3

Table 2: The error norms (25) and (26) for the reference simulation at $t = 1, 3$ and 7.

4. Remarks

We presented the enticing abstract problem of a 3D parabolic drop, with a compact elliptical support, spreading under gravity on the plane. Mathematically, the drop evolution is described by the shallow water equations (SWE), and this paper extends its 2D case introduced in [3]. Here, the relevant theoretical solutions of SWE are derived and analyzed, including the compact closed-form analytical solution for the axisymmetric case. Interesting evolution of the elliptical drop — swapping the initially major and minor axis — is discussed in detail. This peculiar behavior owes to the initial condition that induces larger spreading rates at the steeper slopes in the direction of the minor axis.

The process is accurately reproduced in direct numerical simulation of SWE using the *libmpdata++* — an open-source software library of nonoscillatory forward-in-time solvers for generalized advective transport equations [6]. From the numerical perspective, the presented problem epitomizes inflating-collapsing material layers in isentropic/isopycnic models for atmospheric/oceanic circulations and the evolution of wetting-drying areas in SWE. Consequently, our theoretical solutions provide a convenient testbed for development of relevant numerical methods. In particular, the paper shows that a relatively straightforward implementation of standard monotonicity preserving advection schemes — as described in (22)-(24) — suffices for accurate simulation of wetting-drying areas and, thus, inflating-collapsing material layers [4].

The source code used to obtain the results presented in the paper is freely available at the project repository.[6] It allows to reproduce the analyses and plots presented in sections 2 and 3.

Acknowledgements

We thank Sylwester Arabas for his help with *libmpdata++* and the related software, and Christian Kühnlein for his personal review of the manuscript. DJ acknowledges support from the Polish Ministry of Science and Higher Education (project no. 1119/MOB/13/2014/0). AJ acknowledges support from Poland's National Science Centre (Narodowe Centrum Nauki) [decision

[6] Git repository at `https://github.com/igfuw/shallow-water-elliptic-drop` . All plots and semi-analytical solutions presented in the paper were obtained using Python with external scientific libraries.

no. 2012/06/M/ST10/00434 (HARMONIA)]. PKS acknowledges support by funding received from the European Research Council under the European Unions Seventh Framework Programme (FP7/2012/ERC Grant agreement no. 320375). The National Center for Atmospheric Research (NCAR) is sponsored by the National Science Foundation.

Appendix A. Potential and kinetic energy of elliptical drops

Here we outline the steps leading to the results (11) and (12) obtained in section 2.2.

First, inserting (10) into (8) leads to

$$\mathrm{d}E_{pot} = \frac{1}{2}\frac{1}{\lambda_x^2\lambda_y^2}\left(1-\frac{x^2}{\lambda_x^2}+\frac{y^2}{\lambda_y^2}\right)^2 \mathrm{d}x\mathrm{d}y\ . \tag{A.1}$$

In order to calculate the total potential energy, (A.1) needs to be integrated over the total surface of the drop. For one quadrant of the drop, this is equivalent to integrating over $\mathrm{d}x$ from 0 to $x_{edge} \equiv \lambda_x/\lambda_y\sqrt{\lambda_y^2-y^2}$, and over $\mathrm{d}y$ from 0 to λ_y. Because the potential energy is the same for each quadrant, the latter leads to the total potential energy

$$E_{pot} = 4\int_0^{\lambda_y}\int_0^{x_{edge}} \frac{1}{2}\frac{1}{\lambda_x^2\lambda_y^2}\left(1-\frac{x^2}{\lambda_x^2}+\frac{y^2}{\lambda_y^2}\right)^2 \mathrm{d}x\mathrm{d}y\ . \tag{A.2}$$

Calculating the integrals in (A.2) and manipulating the algebra leads to result (11) in section 2.2.

Second, inserting (10) into (9) gives

$$\mathrm{d}E_{kin} = \frac{1}{2}\left(\dot\lambda_x^2\frac{x^2}{\lambda_x^2}+\dot\lambda_y^2\frac{y^2}{\lambda_y^2}\right)\frac{1}{\lambda_x\lambda_y}\left(1-\frac{x^2}{\lambda_x^2}+\frac{y^2}{\lambda_y^2}\right) \mathrm{d}x\mathrm{d}y\ . \tag{A.3}$$

Because $\dot\lambda_x$ and $\dot\lambda_y$ do not depend on spatial coordinates, the integration over the entire domain results in

$$\begin{aligned} E_{kin} &= 2\dot\lambda_x^2\int_0^{\lambda_y}\int_0^{x_{edge}} \frac{x^2}{\lambda_x^2}\frac{1}{\lambda_x\lambda_y}\left(1-\frac{x^2}{\lambda_x^2}+\frac{y^2}{\lambda_y^2}\right) \mathrm{d}x\mathrm{d}y \\ &+ 2\dot\lambda_y^2\int_0^{\lambda_y}\int_0^{x_{edge}} \frac{y^2}{\lambda_y^2}\frac{1}{\lambda_x\lambda_y}\left(1-\frac{x^2}{\lambda_x^2}+\frac{y^2}{\lambda_y^2}\right) \mathrm{d}x\mathrm{d}y \end{aligned} \tag{A.4}$$

Calculating all integrals in (A.5) gives the relation for total kinetic energy (12) in section 2.2.

References

[1] R. Camassa, D. D. Holm, Dispersive barotropic equations for stratified mesoscale ocean dynamics, Physica D 60 (1-4) (1992) 1–15. doi:10.1016/0167-2789(92)90223-A.

[2] B. Nadiga, L. Margolin, P. Smolarkiewicz, Different approximations of shallow fluid flow over an obstacle., Phys. Fluids 8 (1996) 2066–2077. doi:10.1063/1.869009.

[3] C. Schär, P. Smolarkiewicz, A synchronous and iterative flux-correction formalism for coupled transport equations, J. Comput. Phys. 128 (1996) 101–120. doi:10.1006/jcph.1996.0198.

[4] J. Szmelter, P. Smolarkiewicz, An edge-based unstructured mesh discretisation in geospherical framework, J. Comput. Phys. 229 (2010) 4980–4995. doi:10.1016/j.jcp.2010.03.017.

[5] P. K. Smolarkiewicz, C. Kühnlein, N. P. Wedi, A consistent framework for discrete integrations of soundproof and compressible pdes of atmospheric dynamics, J. Comput. Phys. 263 (2014) 185–205. doi:10.1016/j.jcp.2014.01.031.

[6] A. Jaruga, S. Arabas, D. Jarecka, H. Pawlowska, P. Smolarkiewicz, M. Waruszewski, libmpdata++ 0.1: a library of parallel MPDATA solvers for systems of generalised transport equations, ArXiv e-printsarXiv:1407.1309v2.
URL `http://arxiv.org/abs/1407.1309v2`

[7] C. Frei, Dynamics of a two-dimensional ribbon of shallow water on an f-plane, Tellus A 45 (1) (1993) 44–53. doi:10.1034/j.1600-0870.1993.00004.x.

[8] B. Cushman-Roisin, Exact analytical solutions for elliptical vortices of the shallow-water equations, Tellus A 39 (3). doi:10.1111/j.1600-0870.1987.tb00304.x.

[9] L. Petzold, Automatic selection of methods for solving stiff and nonstiff systems of ordinary differential equations, SIAM Journal on Scientific and Statistical Computing 4 (1) (1983) 136–148. doi:10.1137/0904010.

[10] G. K. Vallis, Atmospheric and Oceanic Fluid Dynamics, Cambridge University Press, Cambridge, U.K., 2006.

[11] P. Smolarkiewicz, L. Margolin, MPDATA: A finite-difference solver for geophysical flows, J. Comput. Phys. 140 (1998) 459–480. doi:10.1006/jcph.1998.5901.

[12] P. Smolarkiewicz, Multidimensional positive definite advection transport algorithm: An overview, Int. J. Numer. Meth. Fluids 50 (2006) 1123–1144. doi:10.1002/fld.1071.